

Perforation of flexible rockfall barriers by normal block impact

J. P. Hambleton^{*1,2}, O. Buzzi², A. Giacomini², M. Spadari² and S. W. Sloan^{1,2}

¹*ARC Centre of Excellence for Geotechnical Science and Engineering, The University of Newcastle, Callaghan, NSW, Australia*

²*Priority Research Centre for Geotechnical and Materials Modelling, The University of Newcastle, Callaghan, NSW, Australia*

Abstract

Flexible rockfall barriers are a common form of protection against falling blocks of rock and rock fragments (rockfall). These barriers consist of a system of cables, posts, and a mesh, and their capacity is typically quantified in terms of the threshold of impact (kinetic) energy at which the barrier fails. This threshold, referred to here as the “critical energy,” is often regarded as a constant. However, several studies have pointed out that there is no single representative value of critical energy for a given barrier. Instead, the critical energy decreases as the block size decreases, a phenomenon referred to as the “bullet effect.” In this paper, we present a simple analytical model for determining the critical energy of a flexible barrier. The model considers a block that impacts normally and centrally on the wire mesh, and rather than incorporate the structural details of the cables and posts explicitly, the supporting elements are replaced by springs of representative stiffness. The analysis reveals the dependence of the critical energy on the block size, as well as other relevant variables, and it provides physical insight into the impact problem. For example, it is shown that bending of the wire mesh during impact reduces the axial force that can be sustained within the wires, thus reducing the energy that can be absorbed. The formulas derived in the paper are straightforward to use, and the analytical predictions compare favorably with data available in the literature.

Keywords: Rockfall barrier; Impact; Kinetic energy; Bullet effect; Finite element; Analytical

* Corresponding author. Address: Civil, Surveying and Environmental Engineering, University of Newcastle, EA215 University Drive, Callaghan, NSW 2308, Australia; Tel.: +61 2 4921 5893; Fax: +61 2 4921 6991
Email addresses: James.Hambleton@Newcastle.edu.au (J. P. Hambleton), Olivier.Buzzi@newcastle.edu.au (O. Buzzi), Anna.Giacomini@newcastle.edu.au (A. Giacomini), Michele.Spadari@uon.edu.au (M. Spadari), Scott.Sloan@Newcastle.edu.au (S. W. Sloan).

1. Introduction

Rockfall protection systems are engineered devices installed in strategic locations to intercept blocks of falling rock along unstable slopes, thereby preventing possible human casualties and damage to sensitive infrastructure. A rockfall protection system generally refers to any interceptive structure and includes walls, berms, catch ditches, and flexible barriers. Among these, flexible barriers are popular for their versatility and effectiveness at arresting blocks and rock fragments over a relatively broad spectrum of sizes. This type of barrier, alternatively referred to as a “catch fence” or “net barrier,” is shown schematically in Fig. 1, and it consists of a wire mesh supported by a system of cables and posts (Peila and Oggeri 2003). The posts are typically anchored to concrete foundations, and the system also can include energy dissipation devices such as friction brakes.

Selecting the design of a flexible barrier is accomplished in two phases. In the first phase, the possible range of block sizes is identified, and the spectrum of impact velocities is subsequently determined from numerical simulations of rockfall trajectories. In the second phase, the dimensions and materials for the barrier are selected such that the barrier can withstand worst-case impacts. Since the severity of the impact increases as either the block size or velocity increases, a barrier’s ability to withstand impact is typically quantified with respect to the impact energy. Generally speaking, the impact energy consists of both translational and rotational kinetic energy. It is common, however, to disregard the rotational kinetic energy and express a barrier’s capacity as the threshold of translational kinetic energy at which the block causes the barrier to fail. In this paper, we refer to this threshold of translational kinetic energy as the “critical energy.”

The critical energy for a flexible barrier is most reliably determined by physical tests (e.g., Smith and Duffy 1990; Hearn et al. 1995; Peila et al. 1998; Grassl et al. 2002; Bertolo et al. 2009; Arndt et al. 2009; Hearn et al. 1992; Buzzi et al. 2012; Peila and Ronco 2009), however large costs and long set-up times have motivated a number studies in which block impact is simulated numerically (e.g., Anderheggen et al. 2002; Cazzani et al. 2002; Volkwein 2005; Cantarelli et al. 2008; Buzzi et al. 2011; Hearn et al. 1995; Hearn et al. 1992). In both tests and simulations, it has been observed that there is no single value of critical energy for a barrier but rather a range of critical energies corresponding to different block sizes. In particular, critical energy decreases as the block size decreases (Cazzani et al. 2002; Volkwein 2005; Cantarelli et al. 2008; Buzzi et al. 2011; Giani 1992; De Col and Cocco 1996; Volkwein et al. 2005). This apparent decrease in barrier performance with block

size is referred to as the “bullet effect,” and its implications can be significant. For example, Cazzani et al. (2002) performed numerical simulations of impact on a full barrier (dimensions 30 m × 3 m) that showed the critical energy dropped as much as an order of magnitude as the block diameter was reduced from 1.3 m to 0.3 m. In practical terms, the implication of the bullet effect is that physical tests or numerical simulations must be conducted for an array of block sizes. This comes at potentially great cost in the case of physical tests, and exorbitant computational times in the case of numerical simulations. Analytical models characterizing this effect are therefore highly desirable. To the authors’ knowledge, none have been attempted.

This paper presents an analytical model for evaluating the critical energy of a flexible rockfall barrier. It is assumed that the block impacts centrally and normally on the wire mesh, as per ETAG207 testing recommendations (EOTA 2008), and that failure occurs within the mesh itself (i.e., mesh perforation). Namely, block impacts on cables and posts are not considered, and variations in the critical energy attributed to the location of impact on the wire mesh are not addressed. It should be noted, however, that central block impact is not necessarily the worst-case scenario, as observed by Cazzani et al. (2002).

To motivate the assumptions of the analytical model, the next section describes the typical pattern of stress and deformation observed within a barrier during block impact. In Section 3, the analytical model is formulated by considering a two-dimensional idealization of the problem and assessing the energy absorbed by the barrier at the point of failure. Section 4 presents observations about the influence of bending of the wire mesh, as well as a corresponding methodology for compensating for bending effects. In Section 5, the analytical predictions are compared with results of finite element simulations from a previous study. Finally, the Section 6 discusses the overall trends predicted by the model and their practical implications.

2. Pattern of stress and deformation during block impact

When a block impacts the wire mesh of a flexible barrier, the impact force is transmitted through the strands of the mesh to the cables and posts. In turn, the forces within the posts are transmitted to the barrier’s foundations. Using a similar conceptual representation as the one presented in the “load path analysis” of Smith and Duffy (1990), Fig. 2 shows the flow of forces during central impact on the middle panel of a three-panel barrier, such as the one illustrated in Fig. 1. Although it is evident that the impact force induces a complex

distribution of stresses within the barrier, the stresses are clearly highest in the region of impact. This is corroborated by the pattern of deformation observed in both physical tests (e.g., Smith and Duffy 1990; Buzzi et al. 2012; Peila and Ronco 2009; Peila et al. 1998) and numerical simulations (e.g., Hearn et al. 1995; Cazzani et al. 2002; Anderheggen et al. 2002; Grassl et al. 2002; Volkwein 2005), where it can be seen the deformation is large in the impacted panel but relatively small in the neighboring panels.

The localized nature of the stresses and deformations during impact suggests that the full details of the barrier can be neglected in the analysis. Rather than model the cables, posts, and foundations explicitly, the barrier can be represented by a region of wire mesh supported on its perimeter by springs of some effective stiffness, as suggested by Spadari et al. (2012). In the representation shown in Fig. 2, the central region of wire mesh is the region of interest, and the stiffness of the springs somehow reflects the stiffness of the cables and wire mesh supporting the region on each edge. The validity of such an approximation depends largely on the force-displacement relationship (linear or nonlinear) specified for the springs and the distribution spatially over the region's perimeter. As in the work of Spadari et al. (2012), it is assumed for simplicity that the region is rectangular, and it is supported on all edges by linear springs with constant stiffness K . The stiffness K is selected so as to reflect the effects of elastic deformation, plastic deformation, frictional interaction of components, and deformation attributed to energy dissipation devices. This is clearly approximate, especially since the latter effects are nonlinear, however the aggregated contributions often can be represented reasonably well.

Utilizing the assumptions discussed above, Spadari et al. (2012) performed simulations of block impact with numerous different mesh properties, block sizes, and values for the effective stiffness K . The simulations were performed using the dynamic finite element code ABAQUS/Explicit by representing the block as an elastic solid and the mesh as a network of rigidly connected beam elements of circular cross section. The geometry of the block was selected as the one suggested by ETAG207 testing guidelines (EOTA 2008), and it impacted with a specified initial normal velocity at the center of the mesh. The overall geometry of the mesh was selected to represent a chain-link configuration, wherein intersecting strands of the mesh form diamond-shaped cells. The block was an elastic solid (Young's modulus of 30 GPa and Poisson's ratio of 0.3), and the wire mesh possessed fixed elastic properties (Young's modulus of 210 GPa and Poisson's ratio of 0.3) but variable yield strength and wire diameter. The density of the block was 2400 kg/m^3 , and the density of the wire was 7800 kg/m^3 . For the wire, the plastic strain corresponding to failure was set to 10%.

Upon reaching this strain limit, corresponding elements were deleted from the model, such that perforation of the barrier was modeled directly. Further details regarding the simulations are given by Buzzi et al. (2011) and Spadari et al. (2012).

Figure 3 shows the pattern of deformation and the distribution of principal stresses observed in a typical finite element simulation of block impact. The contours of principal stresses reveal a cross-shaped pattern in which the largest stresses are transmitted along stands of the mesh in contact with the block in the direction of the nearest support. This pattern was characteristic of all simulations performed, and it was also observed in the load path analysis of Smith and Duffy (1990) and the numerical simulations conducted by Anderheggen et al. (2002). In terms of the deformation, the wires are stretched much more in the y -direction than the x -direction, as manifested through lower curvature of the mesh in the y - z plane as compared to the x - z plane.

3. Simplified two-dimensional model

In this section, a formula for the critical kinetic energy, denoted by E_c , is derived by considering the energy absorbed by the barrier at the point when the mesh fails. At incipient failure, the energy transferred into the barrier by the block consists primarily of stored elastic energy and energy dissipated by plastic deformation. As discussed in Section 2, the spring stiffness K is chosen so as to account for both elastic and dissipative modes of deformation in the components supporting the wire mesh. For simplicity, dissipation due to plastic deformation within the wire mesh itself is neglected. The total absorbed energy is therefore computed simply as the sum of energy absorbed by the springs and the energy absorbed by elastic deformation of the wire mesh. The critical energy E_c is the total absorbed energy at the point when the stresses within the wire mesh reach the yield stress, such that the mesh fails.

In view of the cross-shaped distribution of stresses observed in Fig. 3, it is reasonable to expect that the full system of wires and springs should behave in a manner similar to the system shown in Fig. 4, where regions of mesh with low axial stress have been removed. In the figure, H is the support length, D_b is the nominal block diameter, S is the wire spacing, and variables A and B characterize the mesh geometry as indicated. In terms of the mesh dimensions A and B shown in Fig. 4, the wire spacing S is given by

$$S = \frac{A}{\sqrt{1 + \frac{A^2}{B^2}}} \quad (1)$$

In the reduced system of Fig. 4, the mesh consists of two intersecting strips, where each strip has an “effective width” denoted by L_e . In light of the pattern observed in Fig. 3, L_e is estimated simply as $L_e \approx D_b$.

By assuming that the two strips behave independently in the reduced system of Fig. 4, and by neglecting variations across the width of the strips, it follows that calculations can be performed on a unit-width basis. Hence, the full three-dimensional problem can be conceptually reduced to the two-dimensional analogue shown in Fig. 5. In the two-dimensional problem, the spring stiffness \bar{K} is the stiffness per unit length, and it can be computed from the individual spring stiffness K and the wire spacing S as

$$\bar{K} = \frac{K}{S} \quad (2)$$

The support length in the two-dimensional problem, denoted by \bar{H} , is taken as the complete length of the wire strands within the three-dimensional problem, and it is computed as

$$\bar{H} = H \sqrt{1 + \frac{A^2}{B^2}} \quad (3)$$

The convention adopted in Eqs. (2) and (3) is that the two dimensional counterparts to the three-dimensional quantities are indicated by $(\bar{\cdot})$, and this convention is maintained throughout this section.

Having reduced the impact problem to the simple two-dimensional configuration shown in Fig. 5, it is straightforward to compute the energy absorbed by the barrier. It is assumed that the energy absorbed within the wires is attributed wholly to uniaxial extension, and that the wires fail in uniaxial tension. In Section 4, the latter assumption will be relaxed, and the effects of bending on the axial force at failure will be considered.

The energy per unit length absorbed by the wire mesh, denoted by \bar{E}_w , is calculated as

$$\bar{E}_w = \frac{1}{2} \bar{K}_w e_w^2 \quad (4)$$

where \bar{K}_w and e_w are, respectively, the stiffness per unit length and the extension of the wire mesh. The energy \bar{E}_w can be equivalently written as

$$\bar{E}_w = \frac{1}{2} \frac{\bar{F}^2}{\bar{K}_w} \quad (5)$$

where $\bar{F} = \bar{K}_w e_w$ is the force per unit length in the wire mesh. The stiffness \bar{K}_w in Eqs. (4) and (5) is calculated from the stiffness of an individual wire, K_w , as follows

$$\bar{K}_w = \frac{K_w}{S} \quad (6)$$

$$K_w = \frac{\pi ED_w^2}{4\bar{H}} \quad (7)$$

where E and D_w are, respectively, the Young's modulus and diameter of the wire.

In Fig. 5, each of the two springs of stiffness \bar{K} absorb the same amount of energy. The absorbed energy of an individual spring, denoted by \bar{E}_k , is calculated as

$$\bar{E}_k = \frac{1}{2} \bar{K} e_k^2 \quad (8)$$

where e_k is the extension of the spring. The force in the springs is the same as that in the wire mesh, such that

$$\bar{F} = \bar{K}_w e_w = \bar{K} e_k \quad (9)$$

Upon combining Eqs. (8) and (9), \bar{E}_k is given by

$$\bar{E}_k = \frac{1}{2} \frac{\bar{F}^2}{\bar{K}} \quad (10)$$

The total energy absorbed by the barrier per unit length, denoted by \bar{E} , is the sum of the energy absorbed by the wire mesh and the energy absorbed by the springs, viz.

$$\bar{E} = \bar{E}_w + 2\bar{E}_k \quad (11)$$

Substitution of Eqs. (5) and (10) into Eq. (11) provides

$$\bar{E} = \frac{1}{2} \left(\frac{1}{\bar{K}_w} + \frac{2}{\bar{K}} \right) \bar{F}^2 \quad (12)$$

Equation (12) gives the energy absorbed by the barrier for any force per unit length \bar{F} , and this energy is limited by force that can be sustained by the wire mesh. The maximum value of absorbed energy (the critical energy per unit length) is attained when $\bar{F} = \bar{F}_y$, where \bar{F}_y is the force per unit length required to cause the wire mesh to yield. Assuming uniaxial tension, \bar{F}_y is related to the force at yield in an individual wire, denoted by F_y , through the following

$$\bar{F}_y = \frac{F_y}{S} \quad (13)$$

$$F_y = \frac{\pi}{4} \sigma_y D_w^2 \quad (14)$$

The critical energy per unit length, \bar{E}_c , is thus

$$\bar{E}_c = \frac{1}{2} \left(\frac{1}{\bar{K}_w} + \frac{2}{\bar{K}} \right) \bar{F}_y^2 \quad (15)$$

The total critical energy E_c is obtained by multiplying the critical energy per unit width \bar{E}_c by the width of effected wire mesh, viz.

$$E_c = 2L_e\bar{E}_c = 2D_b\bar{E}_c \quad (16)$$

where the factor of 2 appears on account of the two strips in Fig. 4. One can combine Eqs. (2), (6), (13), (15), and (16) to obtain the final expression of the critical energy as

$$E_c = \frac{D_b F_y^2}{S} \left(\frac{2}{K} + \frac{1}{K_w} \right) \quad (17)$$

Knowing the critical energy E_c , it is straightforward to compute the velocity required for a block of a given size to perforate the barrier. This velocity, denoted by v_c , is here referred to as the ‘‘critical velocity.’’ The critical energy and the critical velocity are related by

$$E_c = \frac{1}{2} m v_c^2 \quad (18)$$

where m is the mass of the block. The mass m depends on both the size and density of the block, and it is related to the nominal block diameter through

$$m = c \rho D_b^3 \quad (19)$$

where c is a constant and ρ is the block density. The specific value of c , as well as the precise definition of D_b , depend on the block geometry. For the block shown in Fig. 3 and prescribed by ETAG207 testing guidelines (EOTA 2008), the constant c is given by $c = 17/24 \approx 0.71$. Upon combining Eqs. (17)-(19), the final expression for the critical velocity is

$$v_c = \frac{F_y}{D_b} \sqrt{\frac{2}{c \rho S} \left(\frac{2}{K} + \frac{1}{K_w} \right)} \quad (20)$$

4. Effect of bending

In the previous section, a state of uniaxial tension within the wire mesh was assumed. However, observations from physical tests and numerical simulations suggest that significant bending of the wire mesh can occur, particularly in the region of mesh in contact with the impacting block. As an example, Fig. 6 shows a sequence of images taken with a high-speed camera as part of barrier impact tests conducted at The University of Newcastle, Australia. In the moments leading up to perforation of the mesh, it is clear that the wires bend at the edges of the block as the mesh deforms. This bending is also visible in results from numerical simulations (Fig. 3).

The tendency for wires in contact with the block to bend around the block’s edges causes a potentially substantial reduction in the maximum axial force that the wire can

sustain. In particular, the wires are subjected to combined tension and bending. As shown in the Appendix, the axial force at yielding in combined tension and bending, denoted by F_M , can be approximated as

$$F_M = F_y \sqrt{1 - \frac{M}{M_y}} \quad (21)$$

where M is the applied moment and M_y is the moment capacity of the wire in pure bending (zero tension), given as

$$M_y = \frac{1}{6} \sigma_y D_w^3 \quad (22)$$

Supposing that the value of M can be determined, the effect of bending can be easily introduced in the analytical model from Section 3 by replacing F_y in Eqs. (17) and (20) with F_M . Unfortunately, suitable values for M cannot be easily determined from direct analysis of the impact problem. Rather than attempting to evaluate M directly, it is postulated that the severity of the bending effect increases as the angle θ increases, where θ is the mesh deflection angle shown in Fig. 5. Mathematically, this implies

$$\frac{M}{M_y} = f(\theta) \quad (23)$$

where f is an increasing function of θ . The angle θ can be related to the total extension e in the wire mesh and springs as follows

$$\tan \theta = \sqrt{2 \frac{e}{\bar{H}} + \frac{e^2}{\bar{H}^2}} \approx \sqrt{2 \frac{e}{\bar{H}}} \quad (24)$$

where

$$e = 2e_k + e_w \quad (25)$$

Upon combining Eqs. (9), (24), and (25), and setting the force \bar{F} equal to the value required to fail the mesh, $\bar{F} = F_M / S$, the critical angle corresponding to mesh failure, denoted by θ_c , is calculated as

$$\tan \theta_c \approx \sqrt{2 \frac{F_M}{\bar{H}K} \left(2 + \frac{K}{K_w} \right)} \quad (26)$$

where quantities \bar{K} and \bar{K}_w have been replaced with K and K_w in accordance with Eqs. (2) and (6).

Upon specifying the function $f(\theta)$, the full system of equations given by Eqs. (21), (23), and (26) can be used to compute F_M for specified values of F_y , K , K_w , and \bar{H} . In general, this would require the use of a numerical procedure, since F_M appears in both Eq.

(21) and Eq. (26). To simplify the analysis, the critical angle θ_c is therefore approximated by replacing F_M in Eq. (26) with F_y as follows

$$\tan \theta_c \approx \sqrt{2 \frac{F_y}{HK} \left(2 + \frac{K}{K_w} \right)} \quad (27)$$

While the critical angle θ_c is somewhat overestimated by Eq. (27), the error is compensated to a degree by the approximation introduced in Eq. (24), and the estimate of θ_c retains its value as an index of the severity of bending within the mesh.

After replacing F_y with F_M in Eqs. (17) and (20), and substituting the expressions from Eqs. (21) and (23), the final formulas for the critical energy and critical velocity are

$$E_c = \frac{D_b F_y^2}{S} \left(\frac{2}{K} + \frac{1}{K_w} \right) [1 - f(\theta_c)] \quad (28)$$

$$v_c = \frac{F_y}{D_b} \sqrt{\frac{2}{c\rho S} \left(\frac{2}{K} + \frac{1}{K_w} \right) [1 - f(\theta_c)]} \quad (29)$$

A possible form for the function f is discussed in the next section, where predictions based on the analytical model are compared with data from numerical simulations. In all subsequent considerations, the function f is written together with the argument θ_c to be consistent with Eqs. (28) and (29).

5. Comparison with numerical simulations

Spadari et al. (2012) assessed critical velocities for numerous combinations of K , D_b , σ_y , D_w , and S by means of the finite element simulations described in Section 2. For each configuration, the critical velocity v_c was determined iteratively by adjusting the initial velocity of the block until perforation of the mesh occurred. The resolution with which v_c was determined was within 1.4 m/s in all cases.

In Fig. 7, the critical velocities evaluated numerically are compared with the analytical predictions given by Eq. (20), which assumes that the wires within the mesh fail in uniaxial tension. While some scatter is present, the data clusters over a reasonably well defined trend line. The relative error varies between -28% and 147%, and the mean error, calculated from the absolute values of the relative errors, is 42%. It is evident that the approximate model predicts critical velocities that are generally larger than those determined from numerical simulation. In view of the arguments presented in Section 4, this overestimation can be attributed to bending effects. In Fig. 8, the relative error is plotted

against the estimate of the critical mesh deflection angle θ_c given by Eq. (27). Represented in this way, there is still a degree of scatter, but the error plainly increases as a function of θ_c . This trend is consistent with the behavior postulated in Section 4, where it was claimed that the severity of bending increases as θ_c increases.

Incorporating the effect of bending in the analytical model requires specification of the function $f(\theta_c)$. The simplest candidate would be $f(\theta_c) = a$, where a is a constant. However, such a simple expression could not account for the trend observed in Fig. 8. It is therefore assumed that $f(\theta_c)$ can be approximated by the linear expression $f(\theta_c) = a + b\theta_c$, where a and b are constants. Upon determining a and b by minimizing the error between the analytical predictions and the data from finite element simulations, we find

$$f(\theta_c) = 0.04 + 0.09\theta_c \quad (30)$$

With reference to Eq. (23), Eq. (30) implies there is always a bending moment induced during impact, even when the mesh deflection during impact is minimal ($\theta_c \approx 0$).

Figure 9 compares the critical velocities evaluated from Eq. (29) with the data obtained from simulations, taking $f(\theta_c)$ as given by Eq. (30). As compared to the predictions obtained without accounting for the effects of bending (Fig. 7), the scatter is reduced, and the magnitude of the error drops significantly. After modifying the model to include the effect of bending, the relative error varies between -39% and 45%, and the mean error computed in terms of the absolute values of the relative errors is 16%. The ratio F_M/F_y varies between 0.41 and 0.84, and the mean is 0.71. This implies that the axial force at yielding is reduced by roughly 30% on average due to the effects of bending.

Spadari et al. (2012) also synthesized the variables characterizing barrier performance in a scaling relationship involving three dimensionless groups, defined as follows

$$E^* = \frac{\rho v_c^2 H}{K} \quad (31)$$

$$S^* = \frac{K}{H \sigma_y} \quad (32)$$

$$G^* = \frac{D_w}{D_b^{3/4} A^{1/4}} \quad (33)$$

The proposed scaling relationship, referred to as the ‘‘RoBaP model,’’ was found to have the form

$$E^* = \alpha (S^*)^\beta \quad (34)$$

where α and β depend on G^* . Figure 10 shows the numerical data obtained by Spadari et al. (2012) when plotted in terms of E^* and S^* . For each given value of G^* , the trend in the data is well-defined, and the exponent in Eq. (34) is roughly constant, with $\beta \approx -1.5$. Furthermore, it can be seen that an increase in the value of G^* causes an upward shift in the plot.

To facilitate comparison between the analytical model proposed in this paper and scaling relationship of Eq. (34), Eq. (29) can be manipulated into the following form

$$E^* = \frac{\pi^2}{8c} \frac{D_w^4}{D_b^2 SH} \left(2 + \frac{K}{K_w} \right) [1 - f(\theta_c)] (S^*)^{-2} \quad (35)$$

From Eq. (35), it is observed that the exponent on S^* is $\beta = -2$, and the dimensionless group G^* nowhere appears. Rather, the coefficient α depends on the following three dimensionless groups

$$\frac{D_w^4}{D_b^2 SH}, \quad \frac{K}{K_w}, \quad \frac{F_y}{HK} \quad (36)$$

where the last dimensionless group appears in the expression for θ_c (see Eq. (27)). In Fig. 11, the numerical data given by Spadari et al. (2012) is plotted in a manner similar to Fig. 10, except that E^* is normalized by α to account for the combined effects of the three dimensionless groups in Eq. (36). The scatter in the data is similar to the scatter observed for a single value of G^* in Fig. 10, however the data collapses around a single trendline.

6. Discussion

The simplified analytical model presented in this paper provides formulas in which the influence of block size is represented explicitly. Inspection of Eqs. (28) and (29) reveals the following dependence of the critical energy E_c and critical velocity v_c on the block size

$$E_c \propto D_b \quad (37)$$

$$v_c \propto \frac{1}{D_b} \quad (38)$$

where the symbol \propto indicates proportionality. In Eq. (37), the bullet effect manifests itself directly in the proportionality between the critical energy E_c and block diameter D_b . In the analytical model, the critical energy increases in proportion to the block diameter simply because the number of wires that intercept the block grows as the diameter increases (see Eq. (16)). As the number of wires in contact with the block grows, the capacity to absorb energy also grows.

In Figs. 12 and 13, the trends predicted from the analytical model are plotted against the critical velocities and critical energies assessed by Cazzani et al. (2002) based on comprehensive numerical simulations of block impact on a full barrier. A complete quantitative comparison with the data of Cazzani et al. (2002) would require determination of a representative value of stiffness K for the barrier modeled in their study. Rather than perform this step, and attempt to identify suitable values for other parameters, curves of the forms given by Eqs. (37) and (38) are fitted directly. For comparison, the curves corresponding to constant critical energy are also plotted. These are given by

$$E_c \propto D_b^0 \quad (39)$$

$$v_c \propto \frac{1}{D_b^{3/2}} \quad (40)$$

where Eq. (40) follows directly from Eqs. (18) and (19). In a manner consistent with how barrier performance is typically evaluated (cf. Cazzani et al. 2002), the curves in Figs. 12 and 13 are plotted so as to match the points corresponding to the largest block exactly, and the predicted trends are viewed as extrapolations to smaller block sizes.

It is seen in Figs. 12 and 13 that the trends predicted by the approximate analytical model (Eqs. (37) and (38)) agree reasonably well with the data from simulations of a full barrier. On the other hand, the trends corresponding to the assumption of constant critical energy (Eqs. (39) and (40)) provide a poor fit.

The trend in the critical energy E_c predicted by the analytical model has significant practical ramifications. Since the critical energy and the block size are proportional, evaluation of the critical energy for a single block size is sufficient to determine the critical energy for all other block sizes. Thus, the variation in barrier performance over a range of block sizes can be determined from a single measurement, either from physical testing or numerical simulation, thereby eliminating the need for multiple tests.

7. Conclusions

The paper presents a simple analytical model for predicting the impact energy required to perforate a flexible rockfall barrier by normal block impact. This model not only provides physical insight into the impact problem but also predicts the dependencies of critical energy and critical velocity on block size well when compared to data from previous studies on barrier impact. Specifically, the model predicts that the critical energy is proportional to the

nominal block diameter, and that critical velocity is inversely proportional to the nominal block diameter. These predictions are of potentially great value in engineering practice, as they enable an immediate characterization of the performance of a flexible barrier over a range of block sizes, without resorting to costly physical tests or computationally expensive numerical simulations. To fully validate the findings presented in this paper, well-controlled physical tests aimed at evaluating critical velocities over a range of block sizes are needed.

The analytical model developed in this paper relies on a two-dimensional idealization of the full impact problem. It may be possible, however, to develop analytical models that consider a fully three-dimensional mode of deformation. Such models would allow for more accurate assessment energy absorption, and they would possibly enable direct incorporation of structural details of the full barrier (e.g., cables, energy dissipators, and posts).

8. Appendix: Combined tension and bending of a circular member

This appendix is devoted to deriving the maximum tension that can be sustained by a member with a solid circular cross section in the presence of an applied moment. Although the general procedure for evaluating the capacity of members in combined tension and bending is well known (e.g., Jirásek and Bazant 2002), a reference pertaining specifically to a circular member could not be found, and the full derivation is therefore presented here.

Figure 14 shows the distribution of plastic stresses in a circular member in combined tension and bending, assuming a fully plastic stress state (i.e., yield stress σ_y) everywhere in the section. The neutral axis is located at a distance z_n above the centroid of the section, and it divides the section into a region of tensile stress with area A^+ and a region of compressive stress with area A^- (see Fig. 14). Areas A^+ and A^- are given by

$$A^+ = \frac{1}{8}D^2(2\pi - \omega + \sin \omega), \quad A^- = \frac{1}{8}D^2(\omega - \sin \omega) \quad (41)$$

where D is the diameter of the section and central angle ω (see Fig. 14) is related to z_n by

$$\omega = 2 \cos^{-1} \left(\frac{2z_n}{D} \right) \quad (42)$$

The stress distribution must be in equilibrium with the applied tension F and applied moment M , and it follows that

$$F = \sigma_y (A^+ - A^-) \quad (43)$$

$$M = \sigma_y (A^+ z^+ + A^- z^-) \quad (44)$$

In Eq. (44), z^+ and z^- are the distances from the section's centroid to the centroids of the regions of tensile and compressive stress, respectively, and they are given by

$$z^+ = \frac{2D \sin^3\left(\frac{\omega}{2}\right)}{6\pi - 3\omega + 3\sin\omega}, \quad z^- = \frac{2D \sin^3\left(\frac{\omega}{2}\right)}{3\omega - 3\sin\omega} \quad (45)$$

Upon combining Eqs. (41) and (43)-(45), the applied tension and moment can be expressed as

$$F = \frac{1}{4} \sigma_y D^2 (\pi - \omega + \sin\omega) \quad (46)$$

$$M = \frac{1}{6} \sigma_y D^3 \sin^3\left(\frac{\omega}{2}\right) \quad (47)$$

After some manipulation, angle ω can be eliminated from Eqs. (46) and (47) to arrive at the following expression, which gives tensile force F in terms of the moment M

$$F = \frac{1}{2} \sigma_y D^2 \left\{ \left(\frac{6M}{\sigma_y D^3} \right)^{\frac{1}{3}} \sqrt{1 - \left(\frac{6M}{\sigma_y D^3} \right)^{\frac{2}{3}}} + \cos^{-1} \left[\left(\frac{6M}{\sigma_y D^3} \right)^{\frac{1}{3}} \right] \right\} \quad (48)$$

It is noted that Eq. (46) with $\omega = 0$ gives the maximum tensile force, corresponding to $M = 0$, as

$$F_y = \frac{\pi}{4} \sigma_y D^2 \quad (49)$$

Similarly, Eq. (47) with $\omega = \pi$ gives the maximum moment, corresponding to $F = 0$, as

$$M_y = \frac{1}{6} \sigma_y D^3 \quad (50)$$

With the aid of Eqs. (49) and (50), Eq. (48) can be rewritten as

$$\frac{F}{F_y} = \frac{2}{\pi} \left\{ \left(\frac{M}{M_y} \right)^{\frac{1}{3}} \sqrt{1 - \left(\frac{M}{M_y} \right)^{\frac{2}{3}}} + \cos^{-1} \left[\left(\frac{M}{M_y} \right)^{\frac{1}{3}} \right] \right\} \quad (51)$$

Lastly, it is noted that Eq. (51) can be approximated by the much simpler expression

$$\frac{F}{F_y} = \sqrt{1 - \frac{M}{M_y}} \quad (52)$$

The normalized axial force F/F_y evaluated from Eq. (52) is less than the value obtained from Eq. (51), but the maximum difference between the two curves over the full range of possible moments, $0 \leq M/M_y \leq 1$, is less than 4%. For comparison, both curves are plotted in Fig. 15.

Acknowledgments

Financial support provided by the ARC Centre of Excellence for Geotechnical Science and Engineering (grant number CE110001009) is gratefully acknowledged. The first and last authors would also like to acknowledge support provided by the ARC Laureate Fellowship entitled “Failure Analysis of Geotechnical Infrastructure” (grant number FL0992039).

References

- Anderheggen E, Volkwein A, Grassl H (2002) Numerical simulation of highly flexible rockfall protection systems. In: Proceedings of the Fifth World Congress on Computational Mechanics (WCCM V), Vienna, Austria
- Arndt B, Ortiz T, Turner AK (2009) Colorado’s full-scale field testing of rockfall attenuator systems. Transp Res Circular, E-C141. Transportation Research Board, Washington, DC
- Bertolo P, Oggeri C, Peila D (2009) Full-scale testing of draped nets for rock fall protection. *Can Geotech J* 46:306-317. doi:10.1139/t08-126
- Buzzi O, Giacomini A, Spadari M, Fityus S (2011) Numerical modeling of a rock fall mesh perforation upon impact. In: Proceedings of the 13th International Conference of the International Association for Computer Methods and Advances in Geomechanics, Sydney, Australia
- Buzzi O, Spadari M, Giacomini A, Fityus S, Sloan SW (2012) Experimental testing of rockfall barriers designed for the low range of impact energy. *Rock Mech Rock Eng* (in press). doi:10.1007/s00603-012-0295-1
- Cantarelli G, Giani GP, Gottardi G, Govoni L (2008) Modelling rockfall protection fences In: Proceedings of The First World Landslide Forum, Tokyo, Japan
- Cazzani A, Mongiovì L, Frenez T (2002) Dynamic finite element analysis of interceptive devices for falling rocks. *Int J Rock Mech Min Sci* 39:303-321
- De Col R, Cocco S (1996) Motivazioni tecniche ed economiche per la standardizzazione di prove sulle opere paramassi nella Provincia Autonoma di Trento. In: Giornata di studio su “La protezione contro la caduta di massi dai versanti rocciosi”. GEAM, Torino, pp 65–72

- EOTA (2008) Guideline for European technical approval of falling rock protection kits (ETAG 027), February 2008, Brussels. <http://www.eota.be/en-gb/content/endorsed-etag-s/9/>
- Giani GP (1992) Rock slope stability analysis. Balkema, Rotterdam
- Grassl H, Volkwein A, Anderheggen E, Ammann WJ (2002) Steel-net rockfall protection - experimental and numerical simulation. In: Proceedings of the Seventh International Conference on Structures Under Shock and Impact, Montreal, Canada
- Hearn G, Barrett RK, Henson HH (1995) Testing and modeling of two rockfall barriers. *Transp Res Rec*, 1504:1-11
- Hearn G, Barrett RK, McMullen ML (1992) CDOT flexpost rockfall fence development, testing, and analysis. *Transp Res Rec*, 1343:23-29
- Jirásek M, Bazant ZP (2002) *Inelastic Analysis of Structures*. John Wiley & Sons, Hoboken
- Peila D, Oggeri C (2003) The use of rockfall protection systems in surface mining activity. *Int J Surf Min Reclam Environ* 17:51-64. doi:10.1076/ijsm.17.1.51.8625
- Peila D, Pelizza S, Sassudelli F (1998) Evaluation of behaviour of rockfall restraining nets by full scale tests. *Rock Mech Rock Eng* 31:1-24. doi:10.1007/s006030050006
- Peila D, Ronco C (2009) Design of rockfall net fences and the new ETAG 027 European guideline. *Nat Hazards Earth Syst Sci* 9:1291-1298
- Smith DD, Duffy JD (1990) Field tests and evaluation of rockfall restraining nets, final report. California Department of Transportation, Sacramento
- Spadari M, Giacomini A, Buzzi O, Hambleton JP (2012) Prediction of the bullet effect for rockfall barriers: a scaling approach. *Rock Mech Rock Eng* 45:131-144. doi:10.1007/s00603-011-0203-0
- Volkwein A (2005) Numerical simulation of flexible rockfall protection systems. In: Proceedings of the 2005 ASCE International Conference on Computing in Civil Engineering, Cancun, Mexico
- Volkwein A, Melis L, Haller B, Pfeifer R (2005) Protection from landslides and high speed rockfall events: reconstruction of Chapman's Peak Drive. In: Proceedings of the 2005 IABSE Symposium, Lisbon, Portugal

Figures

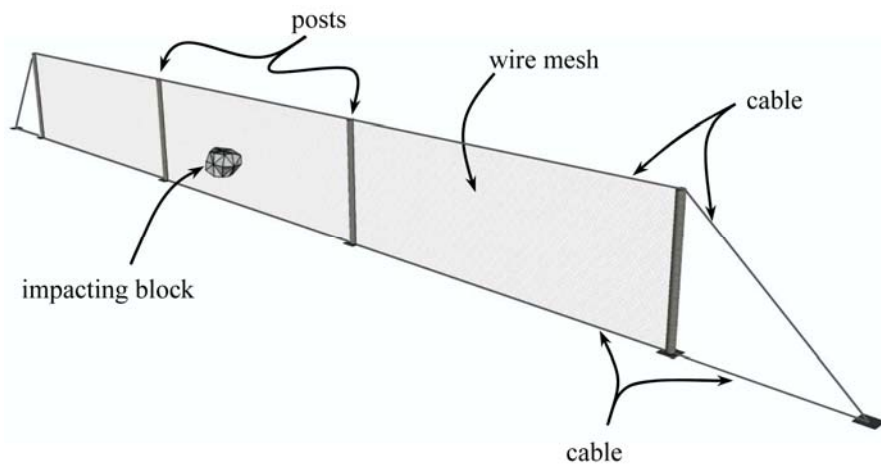


Fig. 1 Schematic of a flexible rockfall barrier

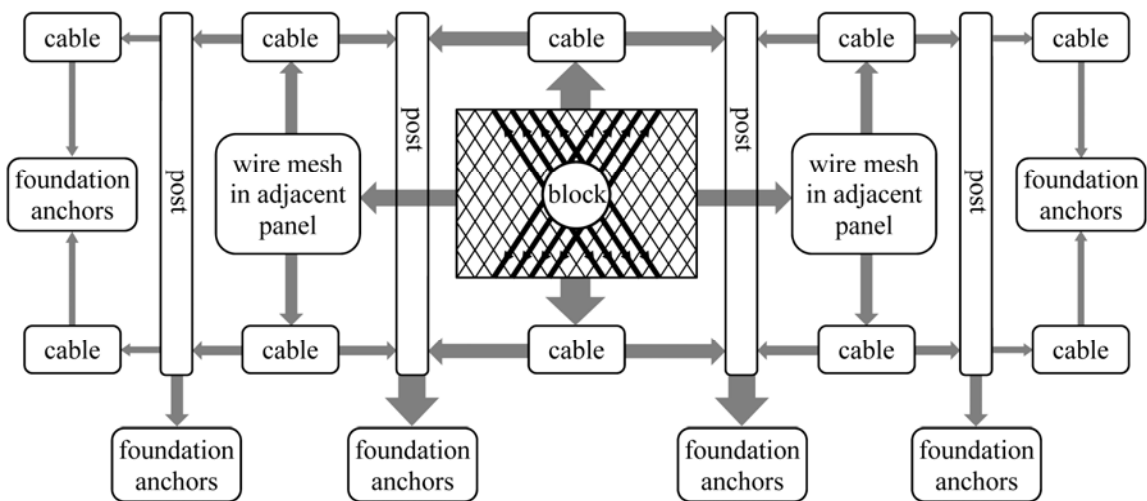


Fig. 2 Flow of forces during block impact on flexible barrier

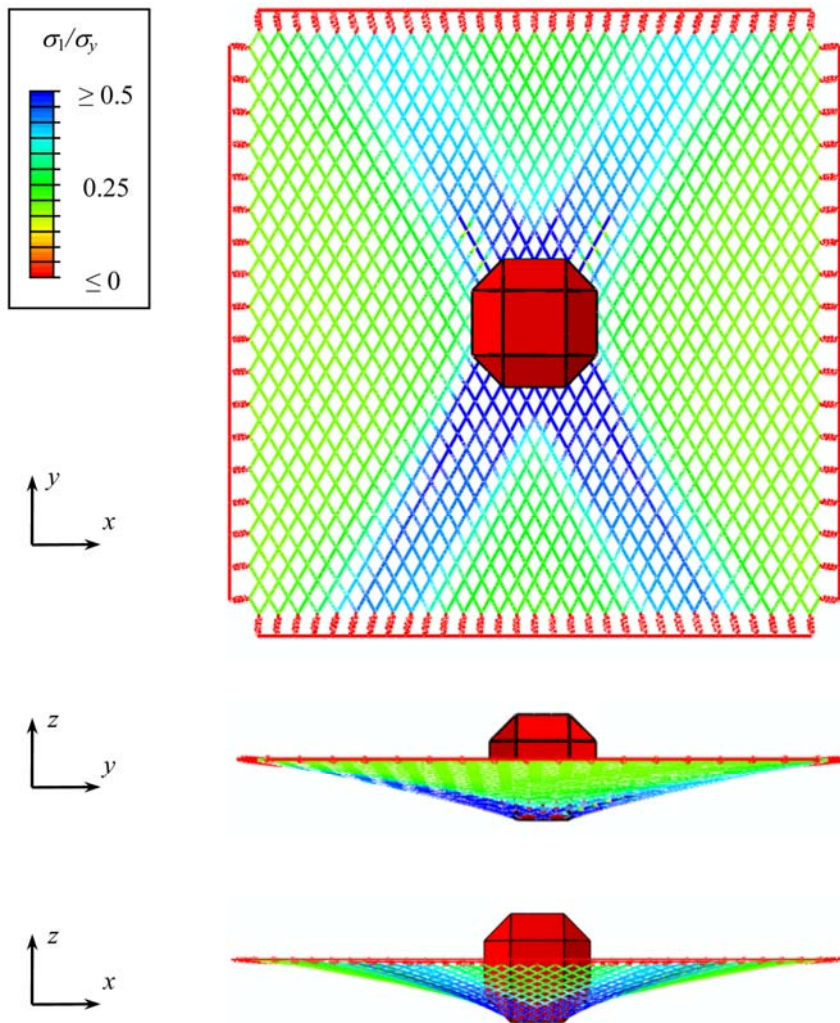


Fig. 3 Deformed configuration from numerical simulation of block impact on a wire mesh supported by springs. Contours show major principal stress in the wires (σ_1) normalized by yield strength (σ_y). At the instant shown, the block moves into the mesh with some velocity, and perforation has not yet occurred

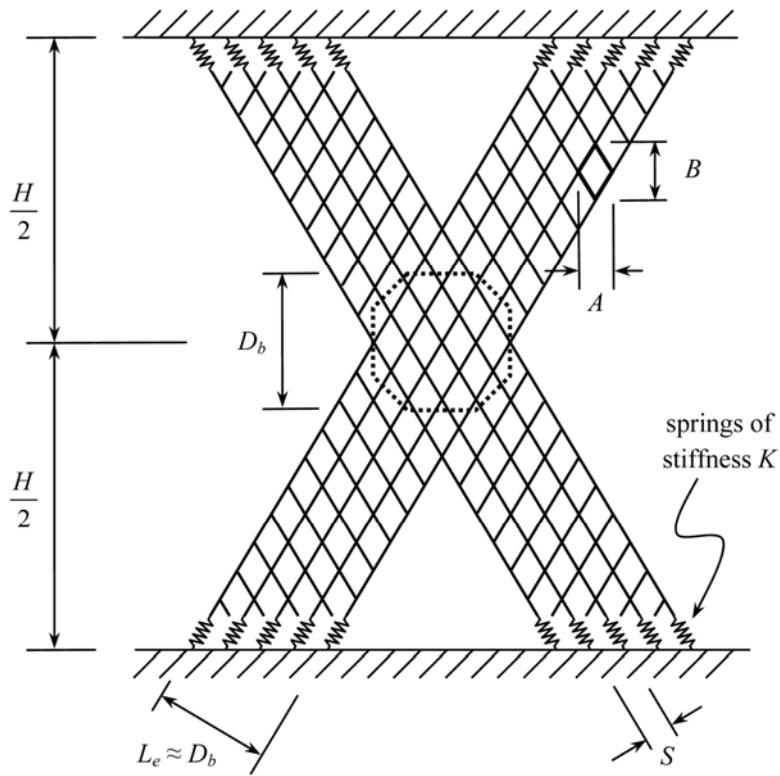


Fig. 4 Cross-shaped region of wire mesh sustaining highest stress levels during block impact

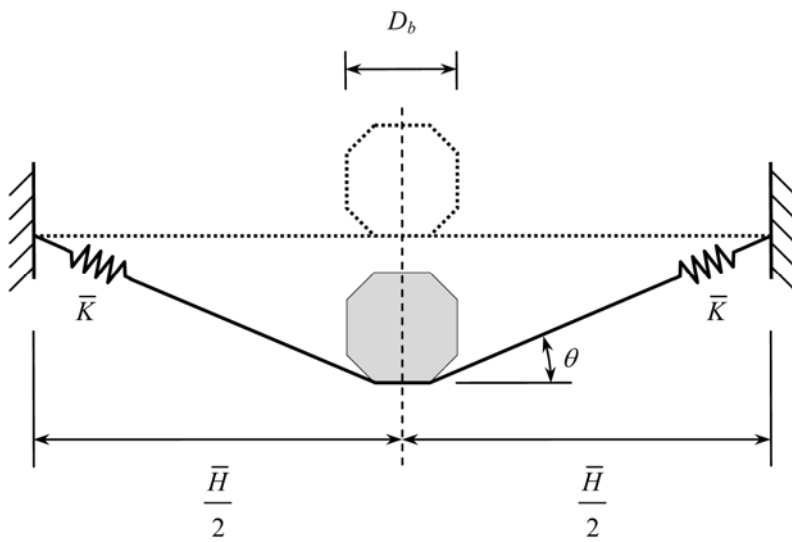


Fig. 5 Schematic of two-dimensional block impact

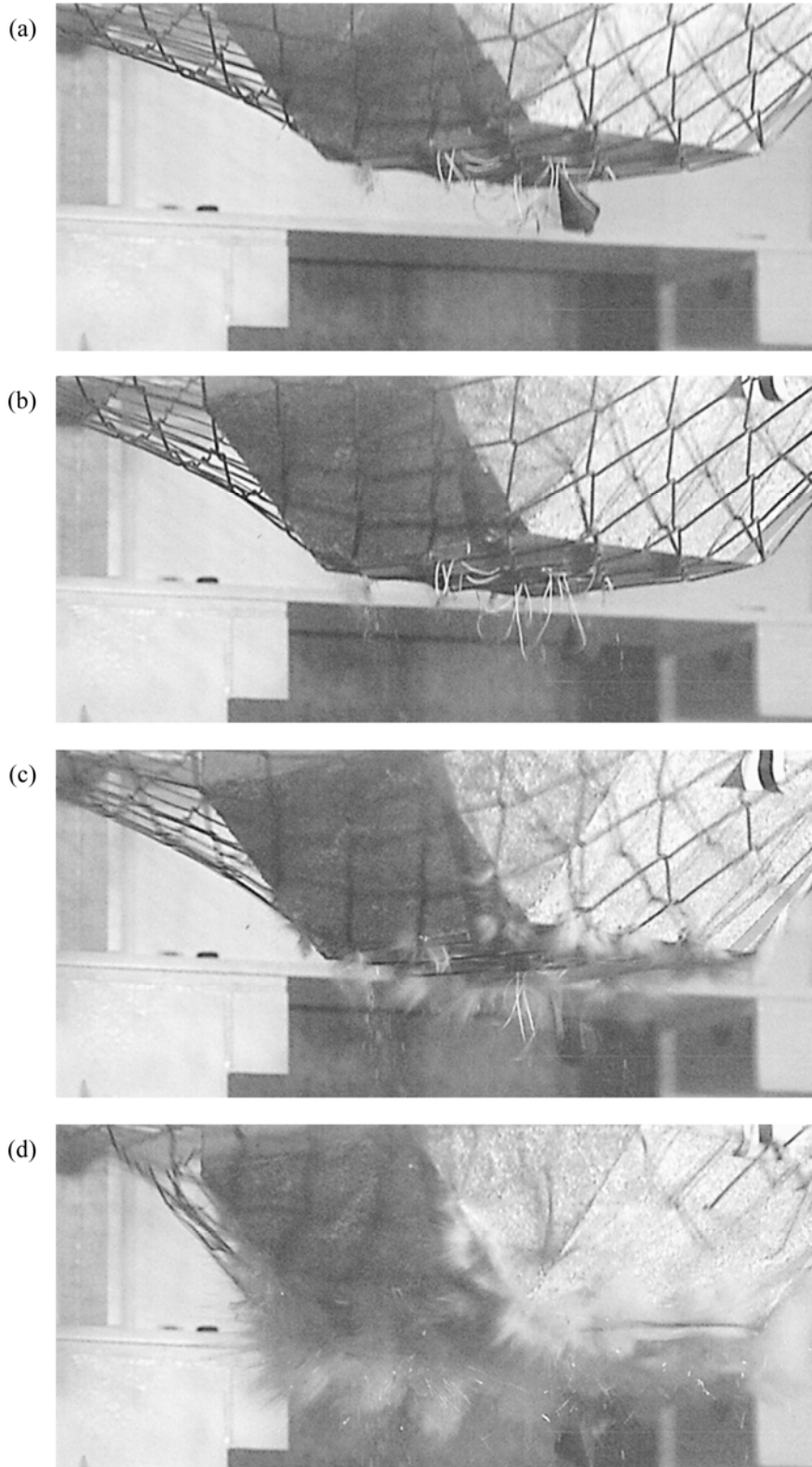


Fig. 6 Sequence of images from high-speed camera showing local mesh deformation during block impact. Subfigures (a) and (b) show the intact mesh moments prior to perforation of the mesh, and (c) and (d) show the post-failure response

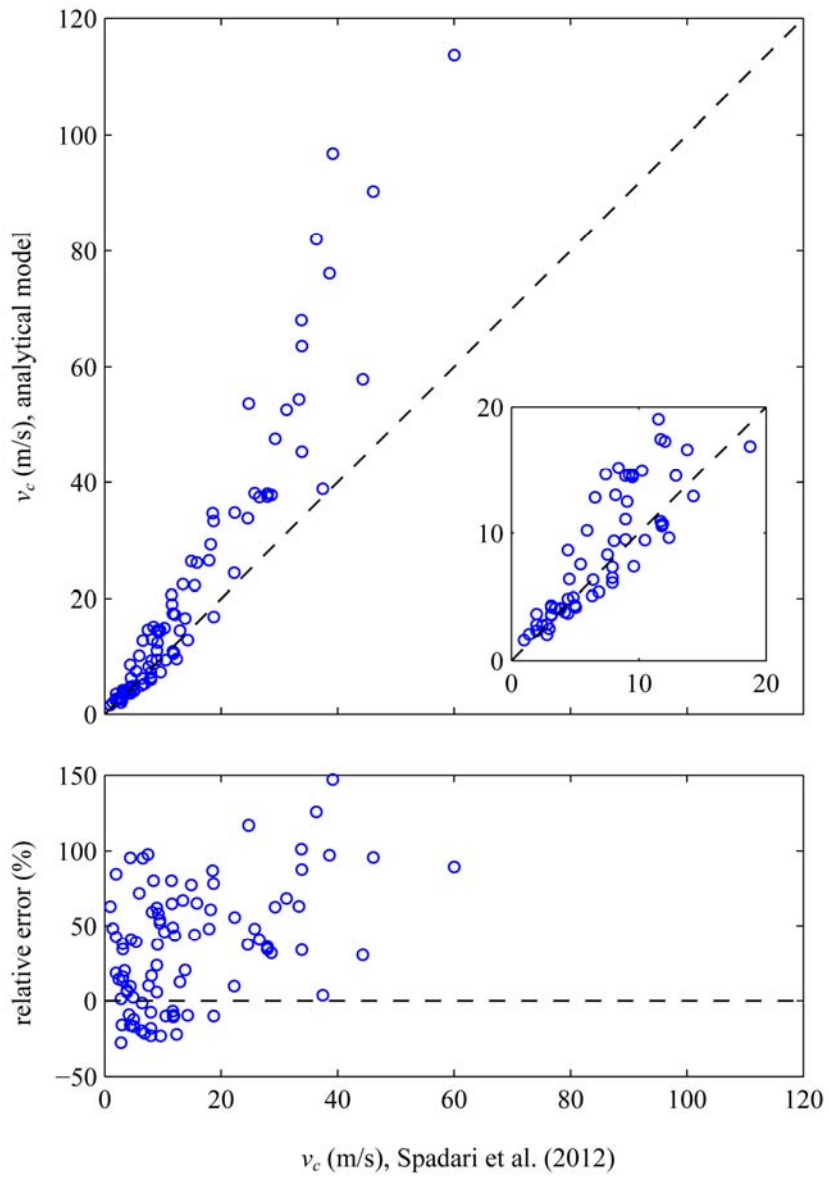


Fig. 7 Comparison of critical velocities from Spadari et al. (2012) and analytical predictions assuming uniaxial tension with the wire mesh

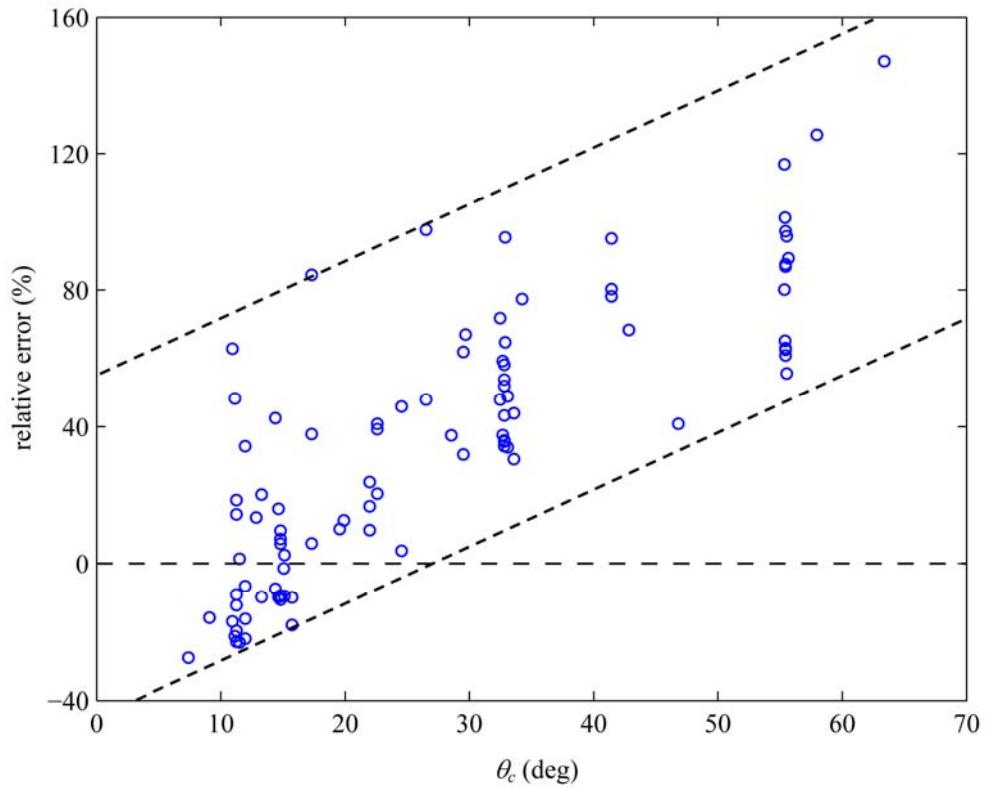


Fig. 8 Relative error in analytical predictions of critical velocity v_c as a function of the critical mesh deflection angle θ_c

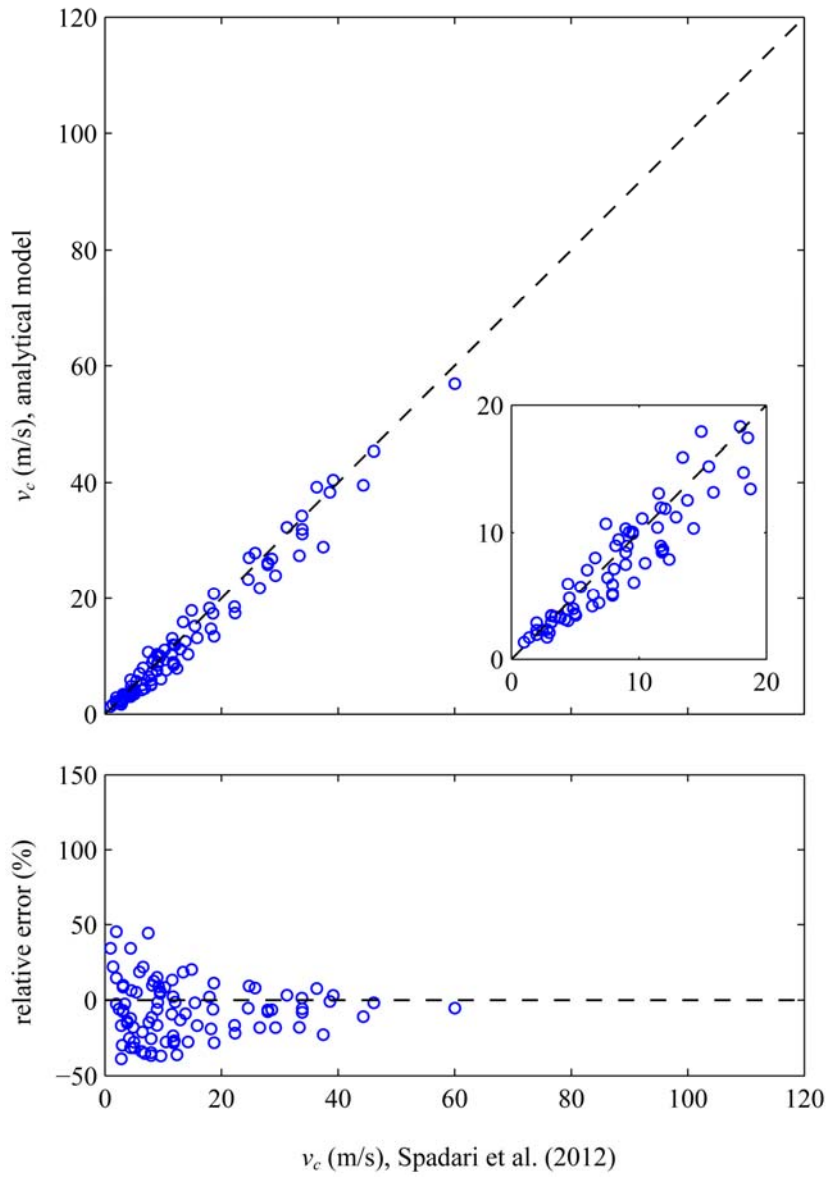


Fig. 9 Comparison of critical velocities from Spadari et al. (2012) and predictions from analytical model with bending

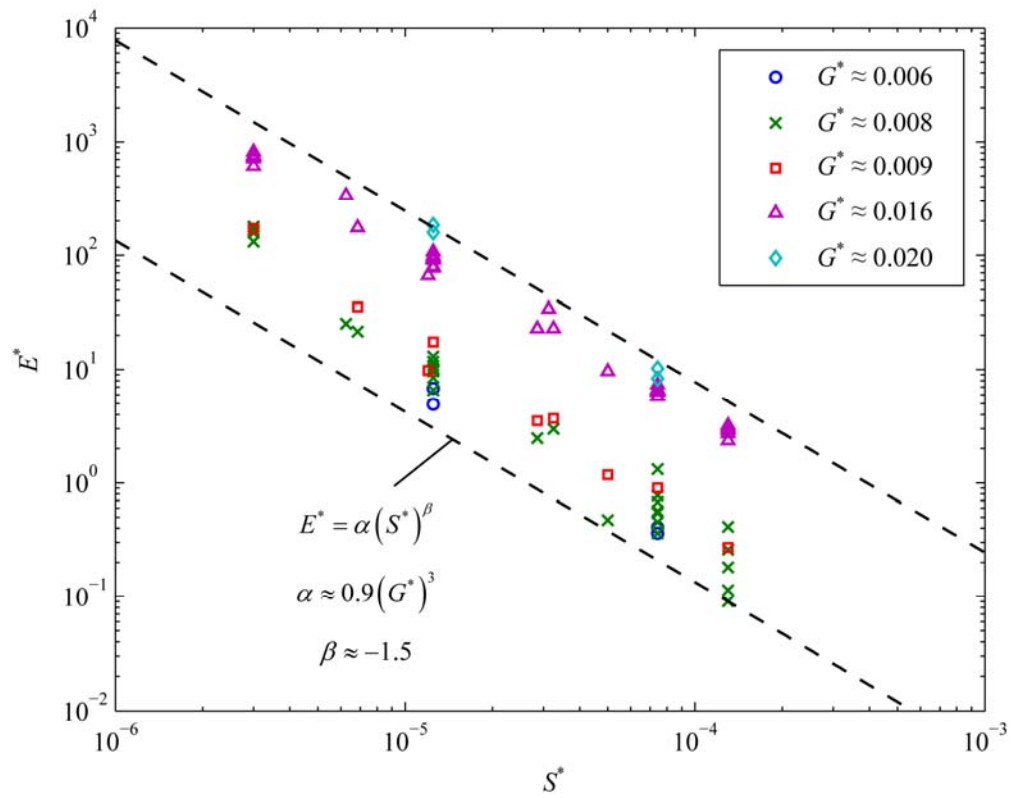


Fig. 10 Relationship between dimensionless groups E^* and S^* for various values of G^* (Spadari et al. 2012)

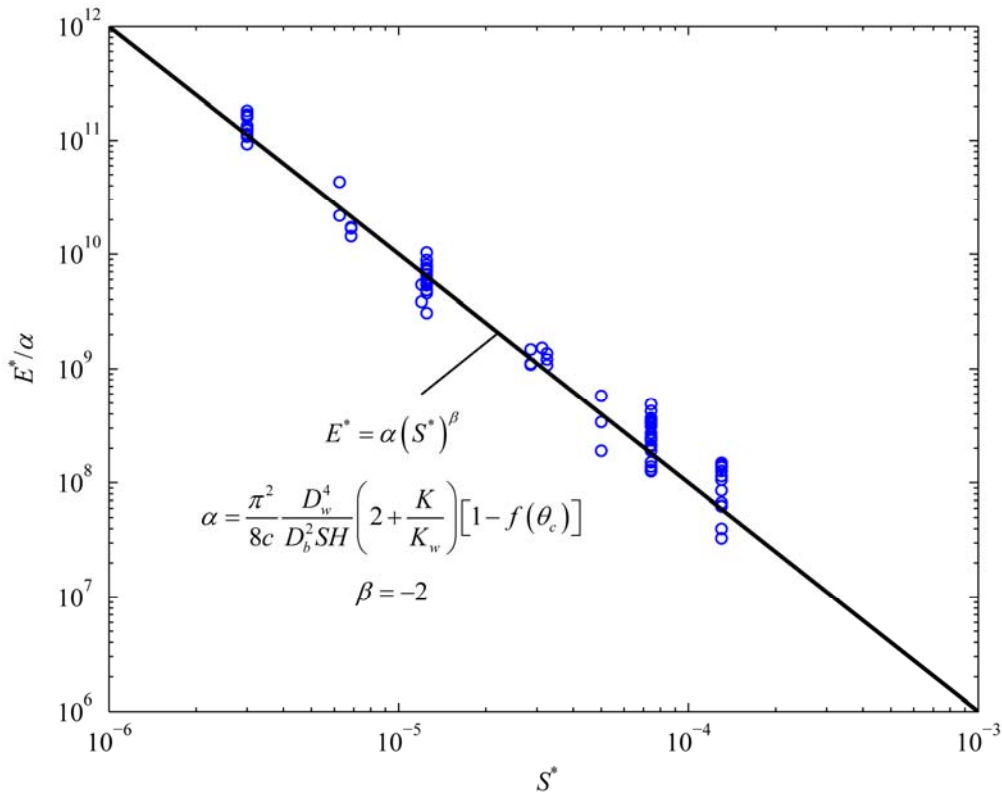


Fig. 11 Relationship between dimensionless groups E^* and S^* as determined from the analytical model

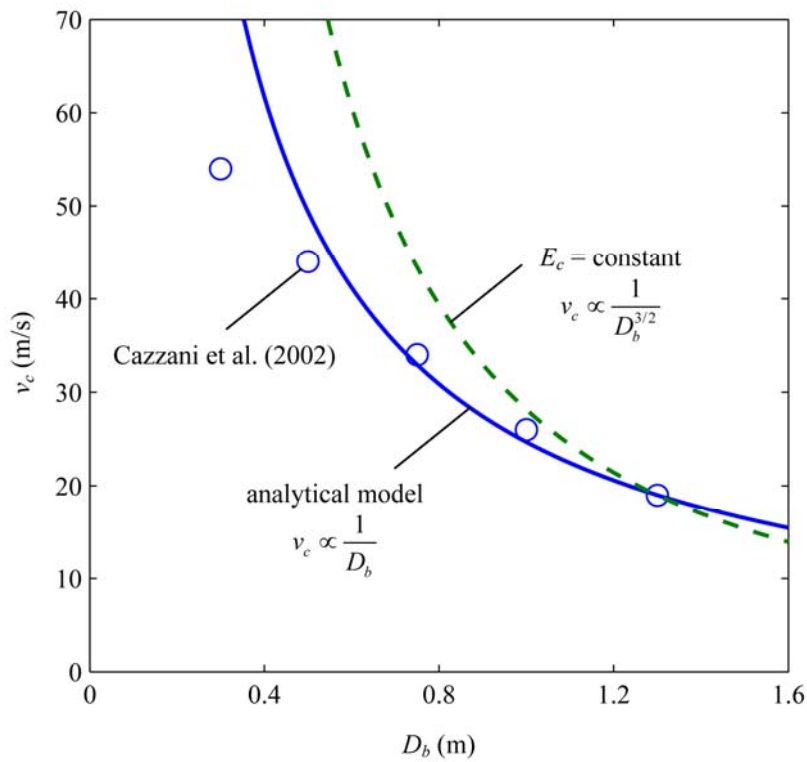


Fig. 12 Critical velocity versus block diameter from Cazzani et al. (2002) with trends corresponding to the analytical model and constant critical energy E_c

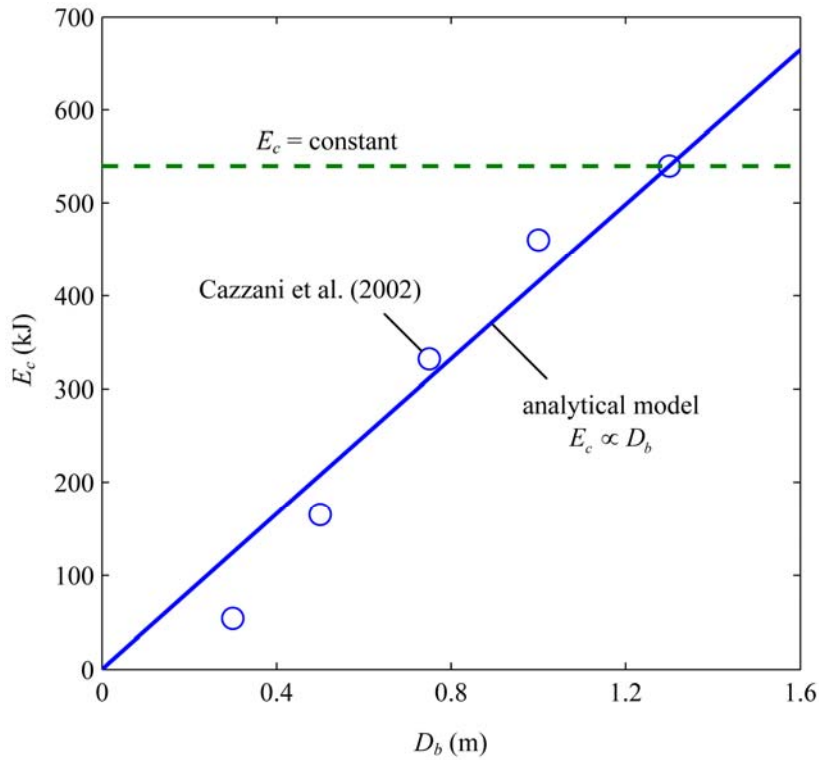


Fig. 13 Critical energy versus block diameter from Cazzani et al. (2002) with trends corresponding to the analytical model and constant critical energy E_c

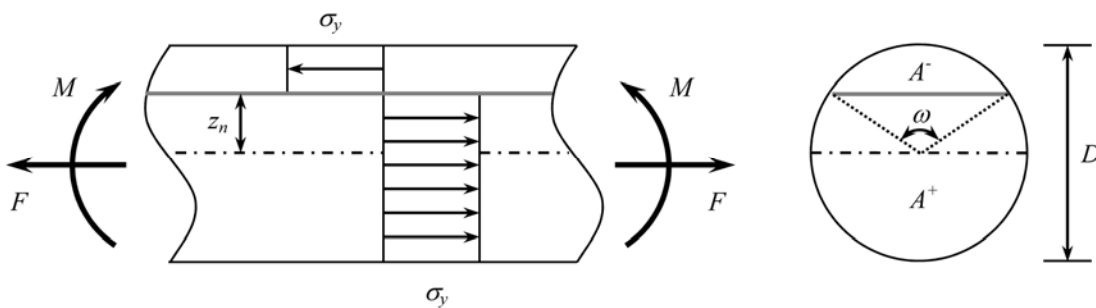


Fig. 14 Plastic stress distribution for a circular member in combined tension and bending

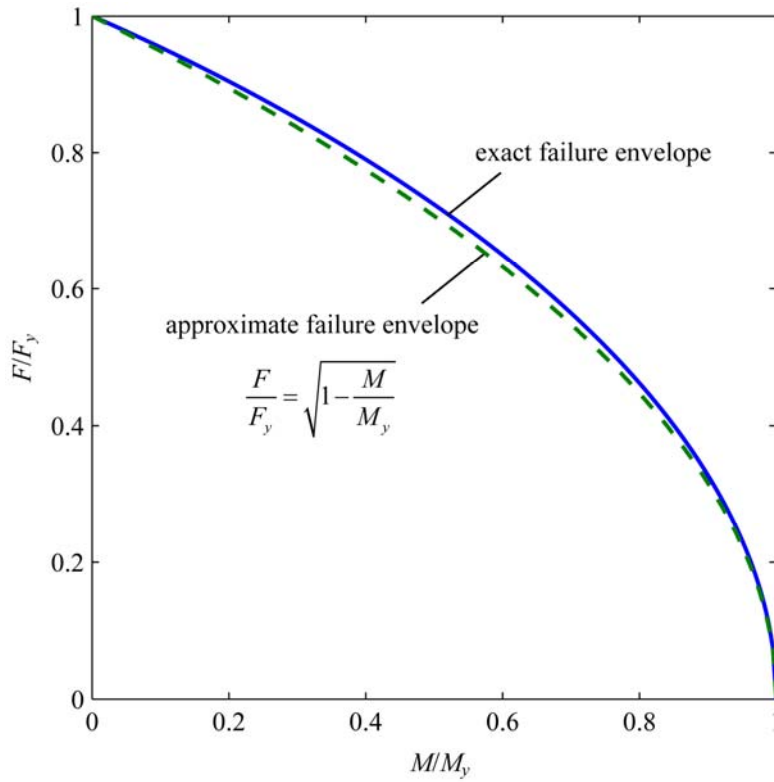


Fig. 15 Exact and approximate failure envelopes for a circular member in combined tension and bending